Biosensors and Bioelectronics 132 (2019) 68–75

Contents lists available at ScienceDirect

Biosensors and Bioelectronics

journal homepage: www.elsevier.com/locate/bios

Electrochemical immunosensors with AuPt-vertical graphene/glassy carbon electrode for alpha-fetoprotein detection based on label-free and sandwich-type strategies

Danfeng Sun[a], Hongji Li[b,*], Mingji Li[a,*], Cuiping Li[a], Lirong Qian[a], Baohe Yang[a]

[a] Tianjin Key Laboratory of Film Electronic and Communicate Devices, School of Electrical and Electronic Engineering, Tianjin University of Technology, Tianjin 300384, PR China

[b] Tianjin Key Laboratory of Organic Solar Cells and Photochemical Conversion, School of Chemistry and Chemical Engineering, Tianjin University of Technology, Tianjin 300384, PR China

ARTICLE INFO

Keywords:
Electrochemical immunosensor
AuPt-vertical graphene
Alpha-fetoprotein
Label-free
Sandwich-type

ABSTRACT

We proposed label-free and sandwich-type electrochemical immunosensors for the quantification of alpha-fetoprotein (AFP), which plays a critical role in the early diagnosis of primary liver cancer. Both detection strategies involved monitoring of the electrochemical response current of the AuPt-vertical graphene (VG)/glassy carbon electrode (GCE) for the oxidation of the redox probe, methyl orange. AuPt nanoparticles, which have good biocompatibility and excellent conductivity, were used to immobilize the primary antibody, Ab_1, while VG sheets helped accelerate electron transfer at the liquid-solid and solid-solid interfaces. The sensing electrode played a key role in signal amplification, and the sensitivity of the sandwich-type sensor was higher than that of the label-free sensor. The former exhibited a wide linear range from 1 fg mL^{-1} to 100 ng mL^{-1} and a low detection limit of 0.7 fg mL^{-1} under the optimal experimental conditions. The excellent performance of the AuPt-VG/GCE-based immunosensors in AFP detection in human serum, coupled with their good stability, makes them promising tools for the clinical monitoring of AFP and other tumor markers.

1. Introduction

Electrochemical immunosensors have been developed for electrochemical analytical methods of quantitative detection of various tumor markers. They are characterized by their fast response, cost effectiveness, and simple operation (Alizadeh et al., 2017). Because common tumor markers, such as alpha-fetoprotein (AFP), carbohydrate antigen 125 (CA-125), CA-15-3, and prostate-specific antigen, are electrochemically inactive, their response signals must be indirectly obtained using a redox probe (Çevik et al., 2016; Gasparotto et al., 2017; Khoshroo et al., 2018; Zhang et al., 2018).

The working electrode and carrier are the main components of electrochemical immunosensors. Improving their fabrication and modification processes can amplify the response signal, thereby increasing the sensitivity of the sensing system. One approach is to immobilize antibodies (Ab's) or antigens (Ag's) using highly biocompatible materials, such as Au (Gasparotto et al., 2017), Pt (Dutta et al., 2017), Ag (Cincotto et al., 2016), and other metal nanoparticles. To control the nanoparticle size, stability in liquid and air, and biocompatibility, a few researchers proposed using a nanohybrid, such as Au@Ag (Zhang et al., 2018) and ZnO nanorod-Au (Gasparotto et al., 2017), which is advantageous to protein immobilization. Most of the carriers that have been used, such as graphene (Khetani et al., 2018; Natarajan et al., 2017), carbon nanotubes (CNTs) (Li et al., 2015), and TiO_2 nanoparticles (Alarfaj et al., 2018), are porous, highly biocompatible, and have a large surface area and high electrocatalytic activity. These carriers can adsorb more metal nanoparticles and prevent agglomeration, thus improving the probe response current. Moreover, they facilitate fast electron transfer and adsorb a significant amount of Ab's or Ag's. The sensitivity of immunosensors can also be significantly increased by creating a strong chemical bond between the metal nanoparticles and carrier, selecting a suitable redox probe, and designing an effective signal amplification strategy (i.e., label-free or sandwich-type) (Akter et al., 2016; Dutta et al., 2017; Serafin et al., 2018).

AFP is a key tumor marker for the early diagnosis of liver cancer patients, who have serum AFP concentrations higher than 25 ng mL^{-1} (Giannetto et al., 2011; Preechakasedkit et al., 2018). A reliable and highly sensitive electrochemical method for the quantitative analysis of

* Corresponding authors.
E-mail addresses: hongjili@yeah.net, lihongji@tjut.edu.cn (H. Li), limingji@tjut.edu.cn, limingji@163.com (M. Li).

https://doi.org/10.1016/j.bios.2019.02.045
Received 3 December 2018; Received in revised form 21 February 2019; Accepted 22 February 2019
Available online 26 February 2019
0956-5663/

AFP in serum not only will play an important role in cancer diagnosis, but also can be further extended to other cancer markers. Label-free and sandwich-type biosensors are commonly used in the quantitative analysis of various tumor markers (Alarfaj et al., 2018; Samanman et al., 2015; Shamsipur et al., 2018). Compared with label-free electrochemical biosensors, sandwich-type ones generally have higher sensitivities because the label helps amplify the electrochemical signal. Hence, it is necessary to further analyze the main differences between the two strategies. We have investigated the sensitivity of various electrochemical immunosensors for AFP detection proposed in recent studies. The best among them were a sandwich-type immunosensor with a sensitivity of 16.07 μA $(\log(\text{ng mL}^{-1}))^{-1}$ (Zhang et al., 2018) and a label-free immunosensor with a sensitivity of 0.42 μA $(\text{ng mL}^{-1})^{-1}$ (Xu et al., 2017).

In this study, label-free and sandwich-type immunosensors for AFP detection were designed and constructed. The sensing platform is vertical graphene (VG) grown on glassy carbon electrode (GCE) modified by electrodeposited AuPt hybrid nanoparticles, and the redox probe was the methyl orange (MO) dye. The AuPt-VG/GCE sensing platform had excellent electrocatalytic activity in the oxidation of MO. The characteristics of the response to AFP in the two detection strategies were analyzed, and the differences between key parameters were compared. This study can serve as a basis for the development of reliable electrochemical immunosensors.

2. Experimental method

2.1. Reagents and solutions

Anti-AFP (Ab_1 and Ab_2), AFP Ag, CEA, CA-199, CA-125, and CA-153 were obtained from Shanghai Linc-Bio Science Co., Ltd. (China). Bovine serum albumin (BSA), dopamine, $HAuCl_4{\cdot}4H_2O$, and citric acid were purchased from Alfa Aesar (USA). The other details are provided in the Supplementary material (SM).

2.2. Morphological and elemental analyses

The morphological characteristics, microstructures, and compositions of the various samples were studied by field-emission scanning electron microscopy (FE-SEM), transmission electron microscopy (TEM), powder X-ray diffraction (XRD), energy-dispersive X-ray spectroscopy (EDS), X-ray photoelectron spectroscopy (XPS), Fourier-transform infrared spectroscopy (FTIR), Raman spectroscopy, and UV–visible spectrophotometry. The details are provided in the SM.

2.3. Electrochemical measurements

Electrochemical experiments, specifically differential pulse voltammetry (DPV) and electrochemical impedance spectroscopy (EIS), were performed on an electrochemical workstation (CHI660E, Chenhua, China). The details are described in the SM.

2.4. Preparation of the AuPt-VG composite on GCE

AuPt-VG/GCE was prepared in two stages: chemical vapor deposition (CVD) and electrodeposition (Fig. 1).

First, to produce VG/GCE, graphene nanosheets are vertically grown on GCE (10 × 20 × 1 mm) via CVD using a DC arc plasma jet system. The GCE is polished to obtain a mirror-like surface using a polishing powder, cleaned by ultrasonication in 1:1 (v/v) HNO_3, ultrapure water, and ethanol for 10 min, and finally, dried under an IR lamp. It is then placed in the CVD reaction chamber, and H_2 and Ar gases are introduced at flow rates of 2 and 1.5 $\text{dm}^3\ \text{min}^{-1}$, respectively. The chamber and pump pressures are maintained at 3000 and 13,000 Pa, respectively. The magnetic field control voltage is set to 6 V (1.57 A) to switch on the device. The arc voltage and arc current are set to 65 V and 116 A, respectively, to form a high-temperature H_2/Ar plasma stream and maintained for 5 min, after which 0.2 $\text{dm}^3\ \text{min}^{-1}$ of CH_4 is introduced into the chamber. The chamber and pump pressures are fixed, and the substrate temperature is controlled at 1100 °C for 5 min.

Subsequently, AuPt hybrid nanoparticles are electrodeposited on the VG layer of VG/GCE. VG/GCE, as the working electrode, forms a three-electrode system with the Pt electrode and SCE. The electrodes are immersed in a mixture of 0.05 mM $HAuCl_4$ and 0.04 mM H_2PtCl_6 and connected to the electrochemical workstation to complete the electrodeposition system. A multi-potential step method is employed for electrodeposition. The initial potential is set to 0 V, the first step potential to 2 V at a step time of 1 s, and the second step potential to −2 V at a step time of 5 s. Thirty cycles (3 min) are run continuously to obtain AuPt-VG/GCE. In addition, this electrodeposition process is repeated in a separate solution of either 0.05 mM $HAuCl_4$ or 0.04 mM H_2PtCl_6 to obtain Au-VG/GCE and Pt-VG/GCE, respectively.

2.5. Preparation of the MO/CNT-Au/Ab_2 label

Fig. 1 shows the preparation of the MO/CNT-Au/Ab_2 label. First, 100 mg of CNT-OH and 500 μL of APTES were dispersed in 10 mL of ethanol. The mixture was stirred and heated at 80 °C for 1.5 h and then dried via suction filtration with ultrapure water to obtain aminated CNT (CNT-NH_2) powder. Subsequently, 100 mg of CNT-NH_2 was dispersed in 10 mL of a mixture of 1.5 mM $HAuCl_4$ and 80 mM citric acid. The Au particles were reduced in situ under UV irradiation at a wavelength of 302 nm and power of 425 W for 3 h to produce CNT-Au powder. CNT-Au powder (250 mg) was then dispersed in 250 mL of 2 mM MO aqueous solution, stirred for 24 h, washed, and dried to obtain MO/CNT-Au powder. Finally, 25 mg of MO/CNT-Au powder was added to 25 mL of 2 μg mL^{-1} Ab_2 solution, stirred at room temperature for 2 h, and then filtered via suction filtration to obtain the MO/CNT-Au/Ab_2 label. The MO/CNT-Au/Ab_2 label was diluted to 2 mL with PBS (pH 7.4) and kept at 4 °C for future use.

2.6. Fabrication of the immunosensors

Ab_1 was immobilized on AuPt-VG/GCE via the interaction between its –NH_2 groups and the AuPt hybrid nanoparticles. First, AuPt-VG/GCE was immersed in 1.5 mL of 500–5000 ng mL^{-1} Ab_1 solution, incubated at 37 °C for 1 h, and dried at room temperature. After incubation, the washed electrode was immersed in 1% BSA solution and incubated at 37 °C for 30 min to prevent nonspecific binding between Ab_1 and AuPt-VG/GCE. Ab_1-AuPt-VG/GCE was washed with PBS (pH 7.4) and covered by 300 μL of AFP Ag solutions of different concentrations and incubated at 37 °C for 0.3–2 h to obtain Ag-Ab_1-AuPt-VG/GCEs (Fig. 1).

2.7. Detection of AFP

Sandwich-type strategy: MO/CNT-Au/Ab_2 (100 μL of 2 μg mL^{-1}) was dropped onto the surface of Ag-Ab_1-AuPt-VG/GCE and incubated at 37 °C for 30 min. The electrode was washed with PBS (pH 7.4) to remove any physically adsorbed MO/CNT-Au/Ab_2 particles. Using MO/CNT-Au/Ab_2-Ag-Ab_1-AuPt-VG/GCE as the working electrode, electrochemical measurements were carried out in 25 mL of 0.1 M PBS at various pH values (Fig. 1).

Label-free strategy: Using Ag-Ab_1-AuPt-VG/GCE as the working electrode, electrochemical measurements were carried out in 25 mL of 0.1 M PBS containing 70 μM MO (Fig. 1).

The oxidation peak of MO is at about 0 V. The response current of the sensors is the oxidation peak current of MO, which, in all cases, was taken as the electrochemical response of MO. Blocking of nonspecific binding sites was performed using 1% BSA solution after each step of the immunological reaction. Dissolved oxygen was dispelled by purging the solution with nitrogen before the measurements.

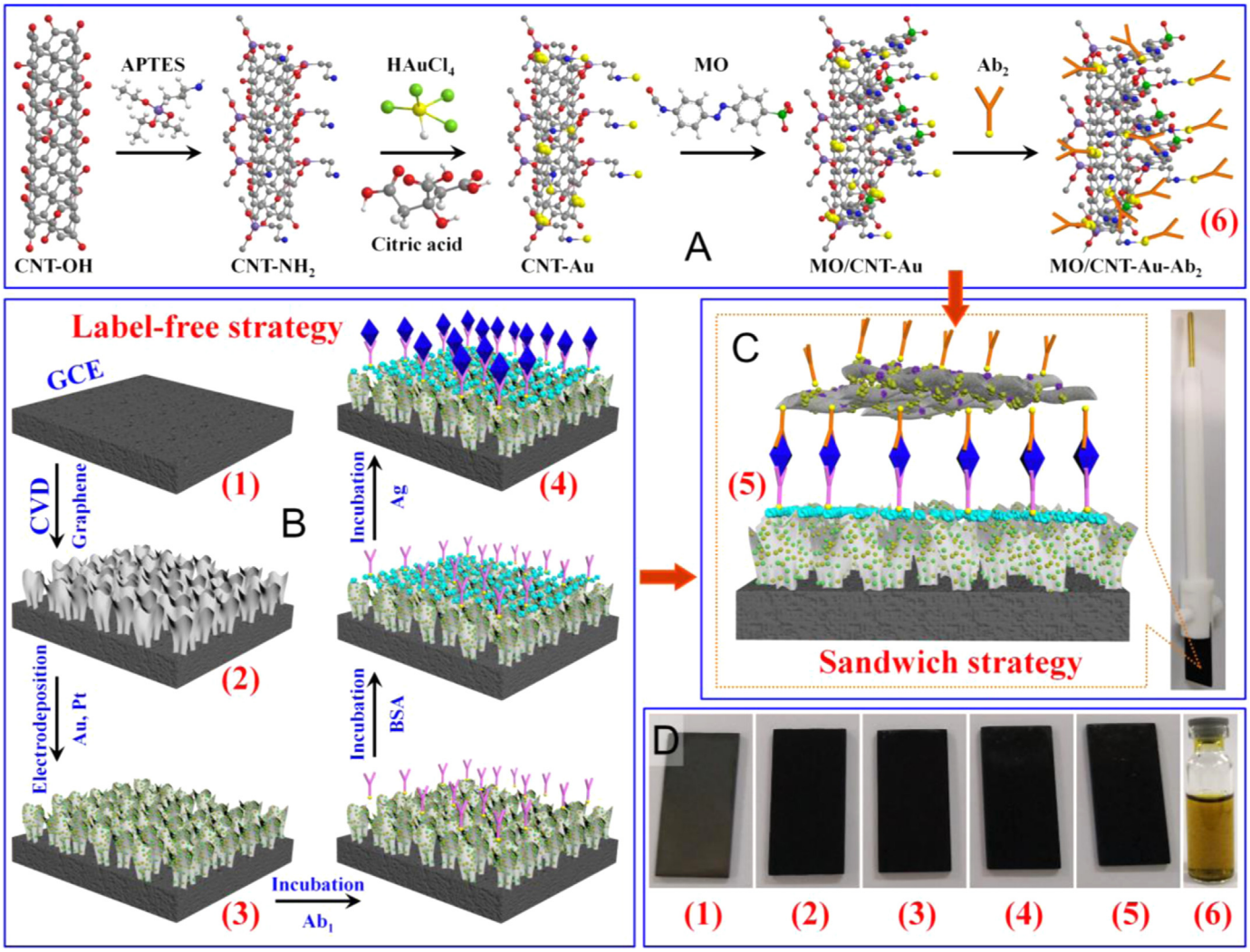

Fig. 1. (A) Preparation of the MO/CNT-Au/Ab_2 label. (B) Schematic diagram of the fabrication of AuPt-VG/GCE-based immunosensor electrodes and label-free strategy for AFP detection. (C) Sandwich-type strategy for AFP detection. (D) Photographs of GCE (1), VG/GCE (2), AuPt-VG/GCE (3), Ag-Ab_1-AuPt-VG/GCE (4), MO/CNT-Au/Ab_2-Ag-Ab_1-AuPt-VG/GCE (5), and MO/CNT-Au/Ab_2 label solution (6).

3. Results and discussion

3.1. Characterization of electrodes and carrier

Fig. 2**A–D** show the SEM images of VG/GCE and AuPt-VG/GCE. The top-view SEM image shows that the VG sheets are staggered in a multi-porous 3D morphology (Fig. 2**A**), while the cross-sectional one shows that they are grown vertically on the surface of the GCE (Fig. 2**B**). Most VG sheets are multilayered (less than 10 layers), as confirmed by the Raman spectrum and high-resolution TEM image (Fig. S1). The SEM images of AuPt-VG/GCE show that AuPt hybrid nanoparticles are uniformly embedded on the surface (Fig. 2**C**), as well as the roots of the VG sheets (Fig. 2**D**). The AuPt hybrid nanoparticles remain firmly embedded on the surface of the VG sheets after ultrasonication in ethanol for 2 h (Fig. 2**E**). The AuPt alloy is characterized by an interplanar spacing of approximately 0.23 nm, which is wider than the Pt (111) plane but narrower than the Au (111) plane (Fig. 2**F**) (Hu et al., 2016).

The composition of the AuPt-VG layer was investigated using SEM-EDS mapping (Fig. S2). The distributions of Pt and Au atoms on the VG sheets are largely the same, and the Pt/Au atomic ratio is approximately 2:1. In another XPS survey spectrum, C, O, Pt, and Au are detected (Fig. 2**G**), and the Pt/Au atomic ratio is consistent with that from the EDS measurements (Fig. S3). The C 1s core spectrum shows peaks at 284.8 eV, corresponding to the C_{sp2}–C_{sp2} bond in the graphene skeleton, and 285.6 eV, corresponding to the C–OR bond associated with the surface adsorbate (Fig. S4A) (Kraus et al., 2016). The peaks at 531.1 and 532.5 eV attributed to the C–O and O–H bonds, respectively, can be distinguished from the O 1s core spectrum (Fig. S4B) (Strauss et al., 2018). In the Pt 4f spectrum, the peaks at 71.3 ($4f_{7/2}$) and 74.6 eV ($4f_{5/2}$) correspond to the Pt^0 state (Fig. S4C), indicating the successful reduction of Pt (IV) (Rettew et al., 2011). The metallic Au^0 state is confirmed by the presence of the Au $4f_{7/2}$ and Au $4f_{5/2}$ peaks at 84.1 and 87.8 eV, respectively, in the Au 4f spectrum (Fig. S4D). The energy level splitting, resulting in a peak-to-peak distance of 3.7 eV, is caused by spin-orbital coupling. This result is consistent with those reported in literature (Abd-Ellah et al., 2016; Jiang et al., 2010; Tian and Tatsuma, 2005).

The SEM image of the CNT-Au nanocomposite, the carrier for MO and Ab_2 in the sandwich-type method, is shown in Fig. 3**A**. Fig. 3**B** shows the XRD patterns of the CNT-OH and CNT-Au carriers. The latter exhibits the characteristic peaks of the (111), (200), (220), (311), and (222) phases of Au at diffraction angles (2θ) of 38.2°, 44.44°, 64.64°, 77.6°, and 81.64°, respectively (JCPDS Card no. 89-3697). The CNT-NH_2 sample obtained by treatment with APTES shows the characteristic peaks of the amino group (–NH_2) in the FTIR spectrum (Fig. 3**C**); the broad band at 3438 cm^{-1} partly overlaps with that of the O–H

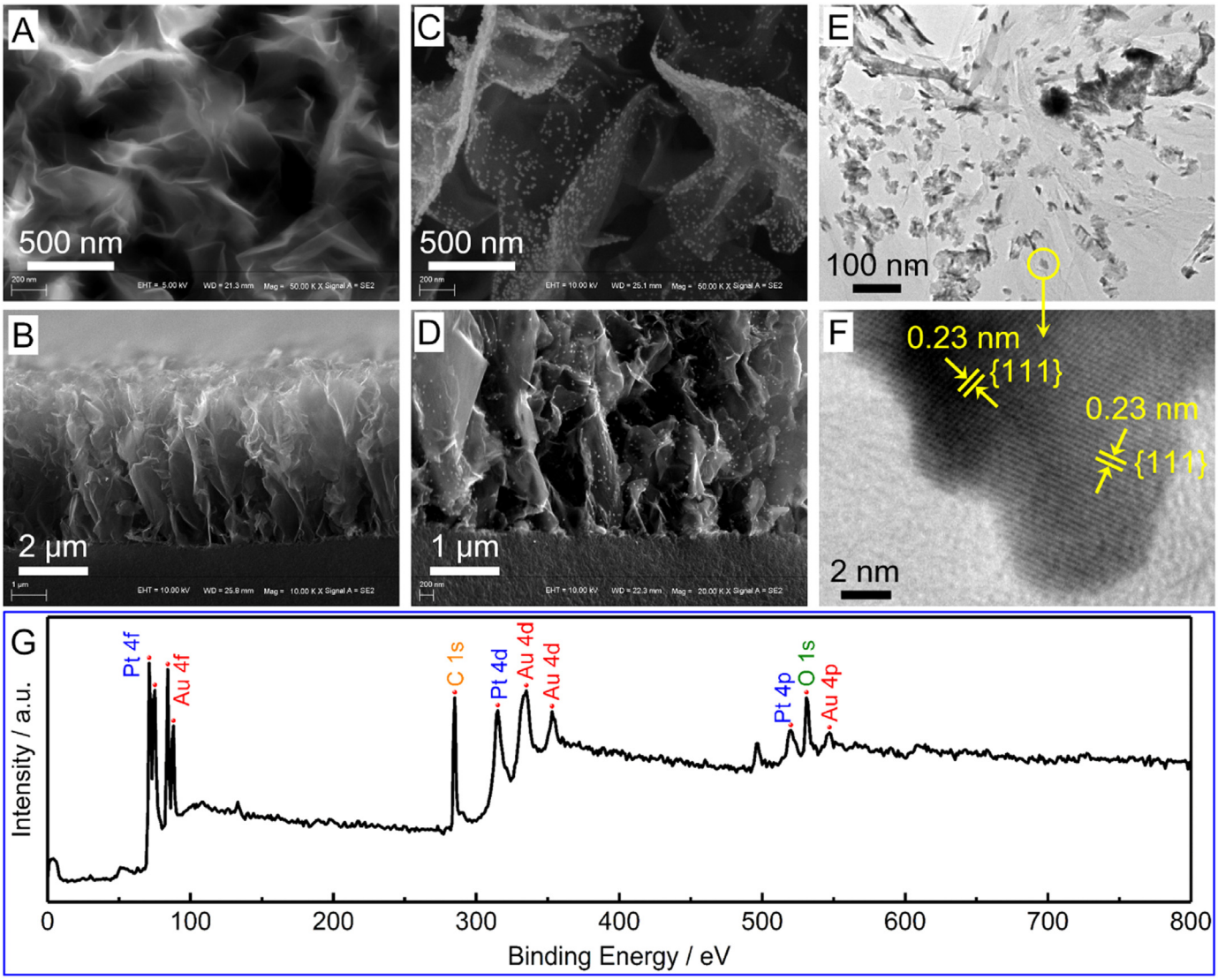

Fig. 2. Characterization of VG/GCE and AuPt-VG/GCE. Surface and cross-sectional SEM images of (A and B) VG/GCE and (C and D) AuPt-VG/GCE. (E) TEM and (F) high-resolution TEM images of AuPt-VG. (G) XPS survey spectrum of AuPt-VG.

stretching vibration, and the band at 1634 cm^{-1} corresponds to the N–H deformation vibration mode (Bogdanowicz et al., 2014). These results, as well as the N 1s core spectrum shown in Fig. 3**D**, confirm the formation of CNT-NH_2. CNT-NH_2 enhances the stability of interactions between Au nanoparticles and CNT via chemical adsorption with the –NH_2 groups. The CNT-Au nanocomposite can adsorb a significant amount of Ab_2 and MO probe molecules owing to its large surface area, while the Au nanoparticles can immobilize the –NH_2 groups of Ab_2, which is an excellent label carrier for the sandwich-type method.

3.2. Analysis and selection of experimental conditions

EIS is widely used to investigate the interfacial properties of electrodes. The Nyquist plots were recorded at each step to investigate the effect of changes in the interfacial state, from the GCE to the final MO/CNT-Au/Ab_2-Ag-Ab_1-AuPt-VG/GCE, on electron transfer kinetics. The corresponding equivalent circuit is given in Fig. 4. It includes the series resistance (R_s) and three circuits. The first circuit includes the interfacial charge-transfer resistance between the electrode and electrolyte (R_{ct} or R_1), Warburg impedance (Z_w), and constant phase element (CPE_1). The second and third circuits include a solid-solid interfacial resistance (R_2 or R_3) and constant phase (CPE_2) or capacitance element (C). The Nyquist plots show a semicircle in the high-frequency region and straight line in the low-frequency region. Intuitively, the semicircle diameter, which is related to R_{ct}, decreases in the order: bare GCE > MO/CNT-Au/Ab_2-Ag-Ab_1-AuPt-VG/GCE > Ag-Ab_1-AuPt-VG/GCE > Ab_1-AuPt-VG/GCE > VG/GCE > AuPt-VG/GCE. The R_{ct} values corresponding to these steps, calculated from the equivalent circuit, are 26.4, 14.5, 12.1, 7.1, 3.0, and 0.01 Ω. The VG on the GCE surface significantly reduces R_{ct} owing to its large surface area, high electrical conductivity, and high electrochemical activity. The AuPt nanoparticles further reduce R_{ct} by improving the electrochemical activity of VG/GCE. However, incubations with Ab_1, Ag, and Ab_2 increase R_{ct} because these proteins are non-conductive and hinder electron transfer. Therefore, we confirmed that the modifications made to the electrode and immunological reaction at each step were successful.

The sensitivity of the sensor depends on the immune response between AFP and anti-AFP on the electrode, which, in turn, depends on the loads and incubation times of Ab_1, the MO/CNT-Au/Ab_2 label, and the Ab_2 conjugated on CNT-Au, and MO concentration. If the amounts of Ab_1 and Ab_2 are significant, the surface conductivity of the electrode will decrease. However, excess Ab_1 can increase the degree of immobilization of AFP and the label, which would increase the response signal for both detection strategies. Almost all AFP immobilized on the

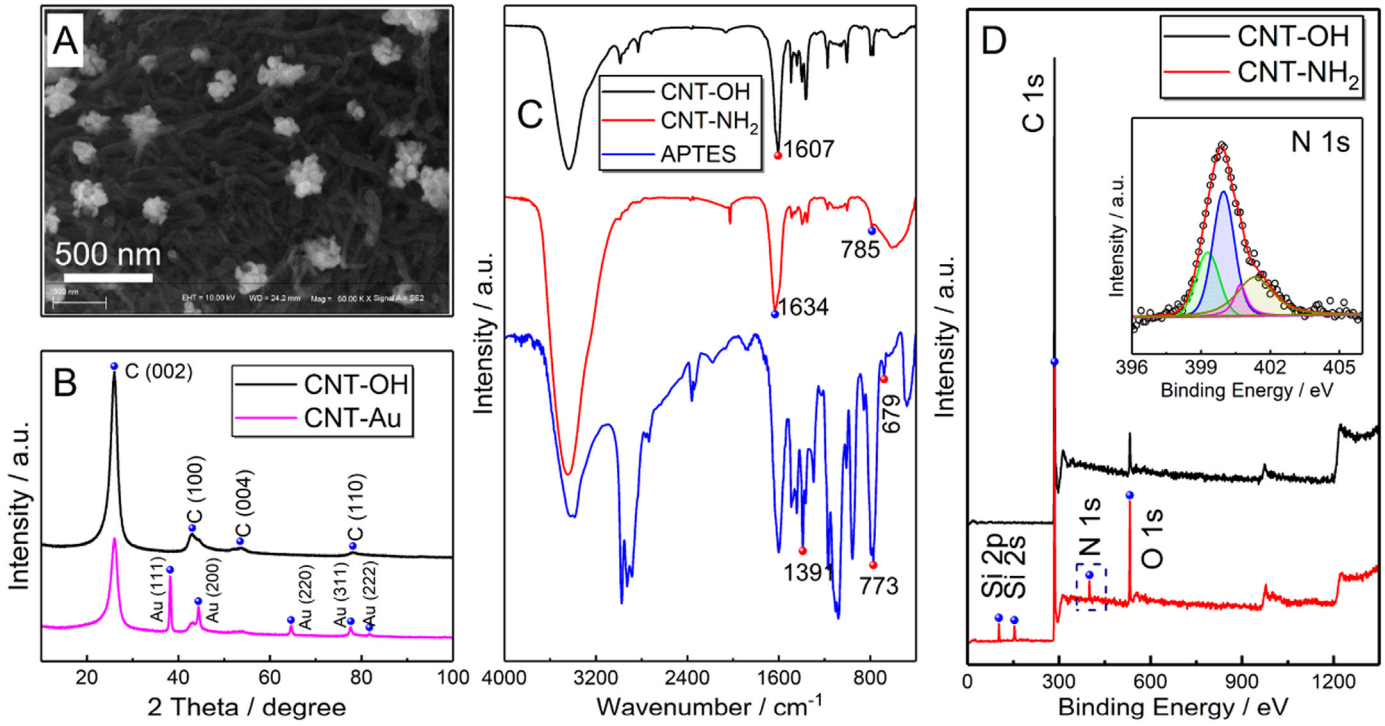

Fig. 3. (A) SEM image of CNT-Au. (B) XRD patterns of CNT-OH and CNT-Au. (C) FTIR spectra of APTES, CNT-OH, and CNT-NH_2. (D) XPS survey spectra of CNT-OH and CNT-NH_2 (inset: N 1 s core spectrum of CNT-NH_2).

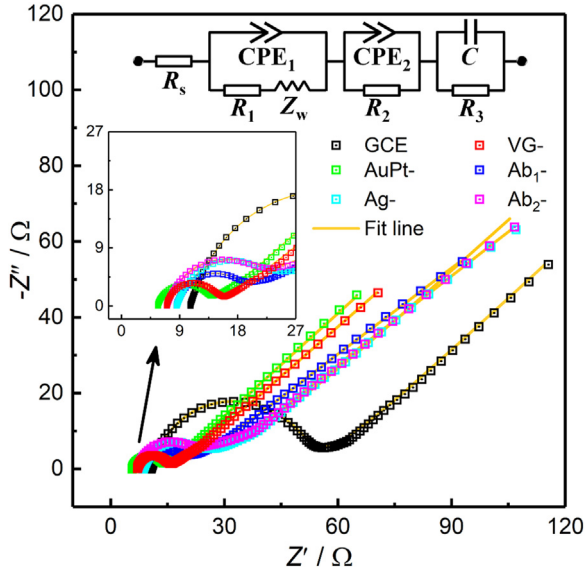

Fig. 4. Nyquist plots from the EIS measurements for bare GCE, VG/GCE, AuPt-VG/GCE, Ab_1-AuPt-VG/GCE, Ag-Ab_1-AuPt-VG/GCE, and MO/CNT-Au/Ab_2-Ag-Ab_1-AuPt-VG/GCE (inset: equivalent circuit used to fit the data and enlarged high-frequency region). The electrolyte was a mixture of 5 mM each of $K_3[Fe(CN)_6]$ and $K_4[Fe(CN)_6]$ in 0.1 M KCl.

electrode can undergo an immunological reaction with the Ab_2 conjugated on CNT-Au. Thus, the experimental conditions, including the Ab_1 concentration, pH, incubation time of the AFP, and MO concentration on the CNT-Au carrier, were optimized to obtain better analytical performance in AFP detection.

In the label-free method, the peak current significantly decreases with an increase in Ab_1 concentration from 0 to 5000 ng mL^{-1}, while in the sandwich-type method, it remains constant within 1000–5000 ng mL^{-1} (Fig. 5**A** and S5). To compare the two methods at a relatively high peak current, the Ab_1 concentration was set to 1000 ng mL^{-1}. The effect of the pH of the PBS solution on the response current at an MO concentration of 70 μM was investigated (Fig. 5**B** and S6). The pH affects the electrocatalytic oxidation of MO by AuPt-VG/GCE. The current signal increases at pH 4–7.5 and then decreases at pH 7.5–9. High acidity or alkalinity may damage the activity of the biomolecules and break the Ag-Ab linkage. Therefore, pH 7.0 was chosen as the optimal pH of the PBS electrolyte in the following experiments. The incubation time of AFP is known to significantly influence the sensitivity of immunosensors. Therefore, the detection of 10 ng mL^{-1} AFP was performed using various incubation times (Fig. 5**C** and S7). For the sandwich-type method, the current response initially increases sharply with an increase in incubation time. However, further increase does not significantly influence the current signal. For the label-free method, the current response decreases sharply with an increase in incubation time. In the label-free method, the response current for MO oxidation decreases because R_{ct} increases with increasing incubation time (Khoshroo et al., 2018). However, with extended immobilization time, more AFP Ag's are loaded onto the electrode surface, leading to high immobilization efficiency (Yin et al., 2017). Therefore, in the sandwich-type strategy, more MO/CNT-Au-Ab_2 labels can be captured by the Ag-Ab_1-AuPt-VG/GCE, resulting in increased electrochemical response. On the other hand, AuPt-VG/GCE becomes saturated with immobilized Ab_1, resulting in a plateau in the electrochemical response. As can be seen from Fig. 5**C**, the response current of the label-free method is much lower than that of the sandwich-type method. To compare the results from the two strategies under the same conditions, an AFP incubation time of 30 min, at which the label-free method has the highest response current, was selected. Furthermore, the absorbance increases sharply with an increase in MO concentration of up to 2 mM; further increase leads to a significant decrease in the absorbance (Fig. 5**D** and S8). Therefore, the probe label was prepared using 2 mM of MO.

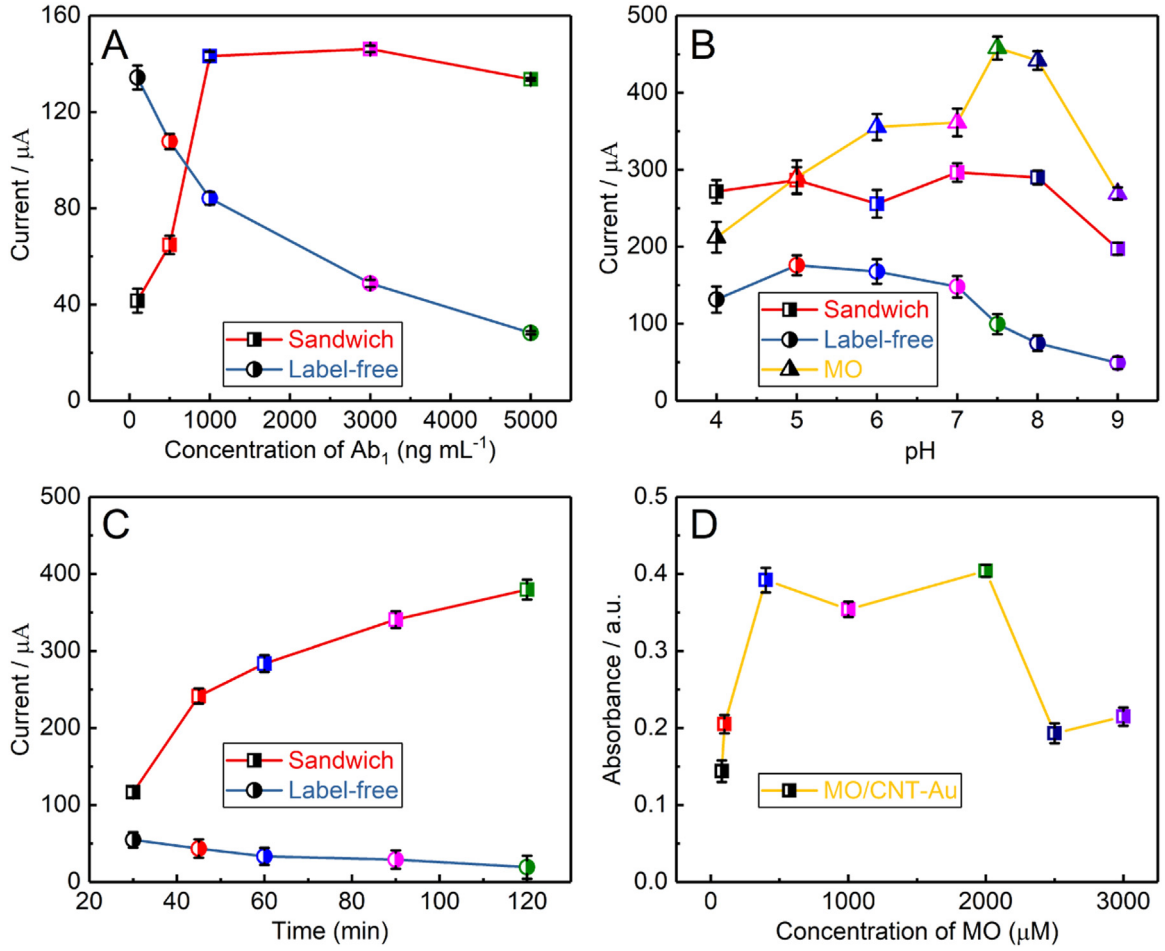

Fig. 5. Optimization of the experimental conditions. (A) Ab_1 concentration. Ab_1, AFP, and Ab_2 were incubated for 60, 30, and 30 min, respectively. (B) pH. The MO concentration was 70 μM, and the incubation times of Ab_1, AFP, and Ab_2 were the same as in (A). (C) Incubation time of AFP. The incubation times of Ab_1 and Ab_2 were the same as in (A). (D) Amount of MO adsorbed per 1 mg mL^{-1} of CNT-Au carrier. The concentration of AFP in (A) to (C) was 10 ng mL^{-1} and that of Ab_1 in (B) and (C) was 1000 ng mL^{-1}. Electrochemical measurements were carried out in 0.1 M PBS and 0.1 M PBS containing 70 μM MO for the sandwich-type and label-free strategies, respectively.

3.3. Detection and analysis

AFP detection was carried out via DPV using AuPt-VG/GCE after condition optimization and analysis. In the sandwich-type strategy, Ag-Ab_1-AuPt-VG/GCE was first incubated in MO/CNT-Au/Ab_2, and the response signals at different AFP concentrations in 0.1 M PBS (pH 7.0) were recorded (Fig. 6**A**). In the label-free strategy, the DPV curves were recorded with the electrodes incubated in different concentrations of AFP in 0.1 M PBS (pH 7.0) containing 70 μM MO (Fig. 6**B**). As the AFP concentration increases, the peak current gradually increases in the former method (Fig. 6**C**) but decreases in the latter method (Fig. 6**D**). The relationship between the logarithm of the AFP concentration and peak current is linear; furthermore, it is proportional for the sandwich-type strategy and inversely proportional for the label-free strategy (Fig. 6**C** and **D**, respectively). For AFP concentrations ranging from 1 fg mL^{-1} to 100 ng mL^{-1}, the regression equations are I (μA) = 43.3 log C (pg mL^{-1}) + 169.1 with a correlation coefficient (R) of 0.996 for the sandwich-type strategy and I (μA) = –33.1 log C (pg mL^{-1}) + 213.1 with an R of 0.990 for the label-free strategy. The sensitivities and detection limits (at a signal-to-noise ratio of 3, details provided in the SM) are 43.3 μA (log(pg mL^{-1}))$^{-1}$ and 0.7 fg mL^{-1}, respectively, for the sandwich-type strategy, and –33.1 μA (log(pg mL^{-1}))$^{-1}$ and 0.9 fg mL^{-1}, respectively, for the label-free strategy. Compared with existing sensors for AFP detection listed in Table S1 (Kavosi et al., 2014; Moazeni et al., 2018; Wang et al., 2018; Xu et al., 2017; Zhang et al., 2018; Zhao et al., 2015), the electrochemical immunosensors fabricated in this work have relatively high sensitivity and lower detection limit.

The excellent performance of the designed sensors may be attributed to two factors: (1) The AuPt nanoparticles ensure the successful conjugation of a significant amount of Ab_1 and the VG sheets ensure electron transfer toward the GCE. (2) The peak current for MO oxidation of the AuPt/GCE-based sensors is very small compared with that of the AuPt-VG/GCE-based sensors (Fig. S9). The AuPt-VG nanosheets are interlaced in a multi-stage, multi-gap network structure and exhibit high electrocatalytic activity for MO oxidation, which result in improved sensitivity of the immunoassay method.

3.4. Reproducibility, specificity, and stability of the immunosensor

To evaluate the reproducibility of the two strategies, we prepared four working electrodes for the detection of AFP (10 ng mL^{-1}) under the same conditions. The relative standard deviations (RSDs) of the measurements are 1.22% and 2.07% for the label-free and sandwich-type methods, respectively (Fig. S10). To confirm the specificity of the two strategies, the current response in the presence of individual interfering substances, including CEA (200 ng mL^{-1}), CA-125 (0.1 kU mL^{-1}), CA-199 (0.1 kU mL^{-1}), and CA-153 (0.1 kU mL^{-1}), was measured. Experiments with and without AFP were performed using the two strategies. Fig. S11 shows that the current variation does not exhibit any significant influence (less than 7%) from the presence of

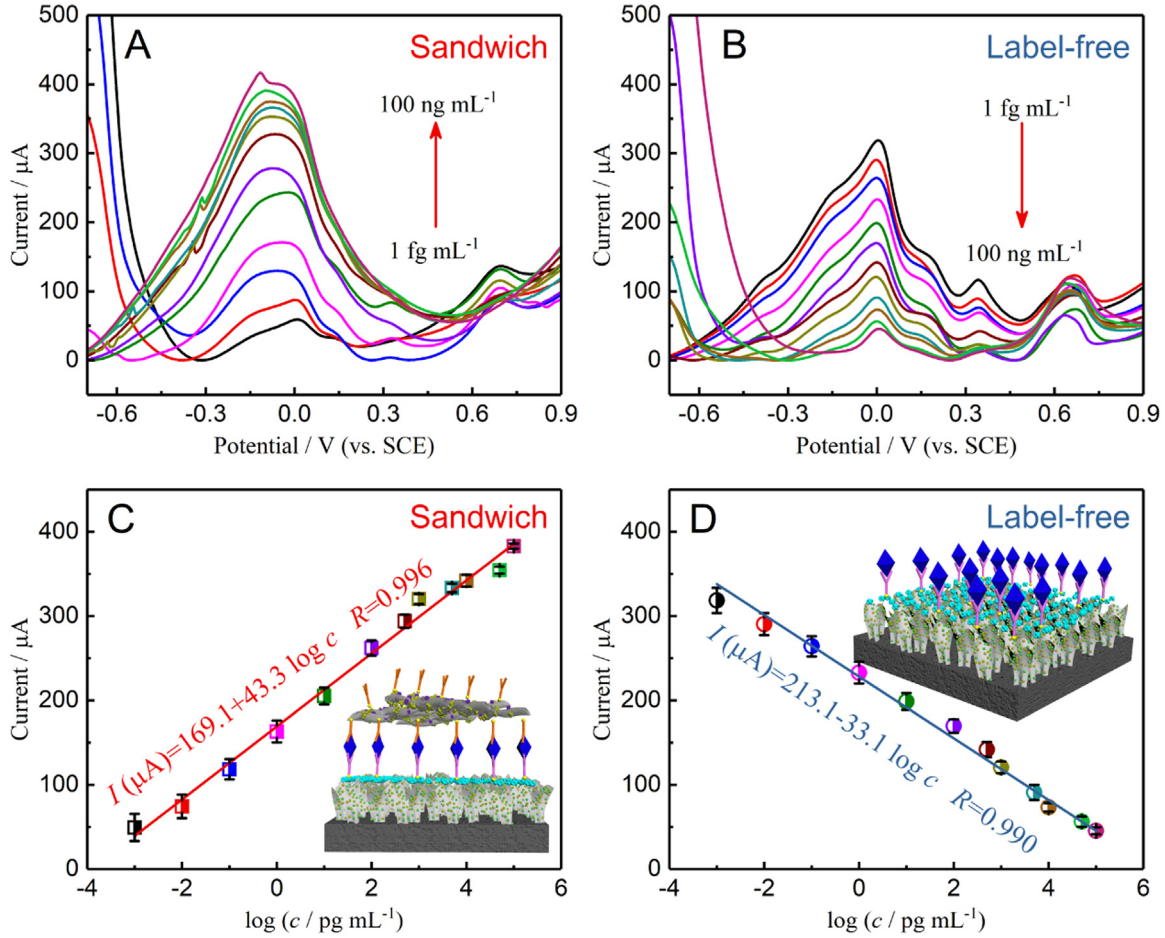

Fig. 6. DPV responses of the (A) sandwich-type sensor in 0.1 M PBS (pH 7.0) and (B) label-free sensor in 0.1 M PBS (pH 7.0) containing 70 μM MO. The AFP concentration ranged from 1 fg mL^{-1} to 100 ng mL^{-1} in both experiments. (C and D) Calibration curves of the two sensors for a range of AFP concentrations [error bars: RSD (n = 5)].

interfering substances.

For samples containing both interfering substances and AFP, the current variation of the label-free method is larger than that of the sandwich-type method. For samples containing only the interfering substances, the current variations of the two strategies are similar. The stability of the two strategies was evaluated by periodically detecting the current responses to AFP. After storing Ab_1-AuPt-VG/GCE at 4 °C for one month, the peak current decreases by 1.5% and 4.0% with respect to the initial value for the sandwich-type and label-free methods, respectively (Fig. S12). This result confirms that the two sensors have good stability.

3.5. Real sample analysis

The reliability of the two strategies for clinical applications was investigated by measuring the AFP concentration in serum. Normal human serum was first diluted to 20 vol% with PBS (pH 7.4). For different amounts of the AFP standard added to the 20% serum solution, the recoveries are 98.2–101.1% and 96.6–100.4% for the label-free and sandwich-type strategies, respectively (Tables S2 and S4). Further, the interference of coumarin (1 μM), curcumin (1 μM), and bergamot essential oil (1%) on the detection of AFP in human serum was investigated. The change in the response current was 1.8–6.7% and 2–5.3% for the label-free and sandwich-type methods, respectively, which are acceptable for real sample application (Fig. S13). Thus, the AuPt-VG/GCE-based AFP detection system can be effectively applied to the clinical monitoring of patients.

3.6. Comparison of label-free and sandwich-type strategies

The label-free and sandwich-type strategies have a similar linear concentration range and percentage recovery for the detection of AFP in human serum. The lack of significant difference between the two strategies is due to the use of the same working electrode. Nevertheless, the sandwich-type method has higher sensitivity and lower detection limit than the label-free method. The layer of immune complex covering the electrode is thicker in the former method (Fig. S14), which reduces the MO probe concentration on the contact electrode surface. Despite this loss, the effective immune response increases under optimal test conditions, which increases several key indicators of the sensor.

4. Conclusions

Sandwich-type and label-free electrochemical immunosensors based on the same signal amplification platform (AuPt-VG/GCE) and redox probe (MO) for AFP detection were designed. AuPt-VG/GCE has a multi-porous 3D morphology and high electrochemical activity, which successfully amplify the electrical signals of the sensors. Both sensors exhibited excellent performance at AFP concentrations ranging from 1 fg mL^{-1} to 100 ng mL^{-1}. In terms of sensitivity and detection limit, the sandwich-type immunosensor [43.3 μA $(\log(\text{pg mL}^{-1}))^{-1}$ and 0.7 fg mL^{-1}, respectively] was superior to the label-free immunosensor. The two sensors exhibited good reproducibility, selectivity, and long-term stability, making them promising tools for tumor marker detection

for clinical diagnosis. Our future research will focus on the detection of different tumor markers using the same sensing platform to develop sensor arrays for the detection of multiple analytes.

CRediT authorship contribution statement

Danfeng Sun: Conceptualization, Methodology. **Hongji Li:** Investigation, Data curation, Writing - original draft. **Mingji Li:** Writing - review & editing, Supervision. **Cuiping Li:** Formal analysis. **Lirong Qian:** Software. **Baohe Yang:** Supervision.

Acknowledgements

We acknowledge support from the Natural Science Foundation of Tianjin City (Nos. 17JCZDJC32600 and 16JCYBJC16300), National Key R&D Program of China (No. 2016YFB0402700), and Youth Top-Notch Talents Program of Tianjin City (No. TJTZJH-QNBJRC-1-13).

Declaration of interest statement

We declare that we have no financial and personal relationships with other people or organizations that can inappropriately influence our work, there is no professional or other personal interest of any nature or kind in any product, service and/or company that could be construed as influencing the position presented in, or the review of, the manuscript entitled, “Electrochemical immunosensors with AuPt-vertical graphene/glassy carbon electrode for alpha-fetoprotein detection based on label-free and sandwich-type strategies”

Appendix A. Supplementary material

Supplementary data associated with this article can be found in the online version at doi:10.1016/j.bios.2019.02.045.

References

Abd-Ellah, M., et al., 2016. Nanoscale 8, 1658–1664.
Akter, R., et al., 2016. Biosens. Bioelectron. 80, 123–130.
Alarfaj, N.A., El-Tohamy, M.F., Oraby, H., 2018. New J. Chem. 42, 11046–11053.
Alizadeh, N., Hallaj, R., Salimi, A., 2017. Biosens. Bioelectron. 94, 184–192.
Bogdanowicz, R., et al., 2014. J. Phys. Chem. C 118, 8014–8025.
Çevik, E., et al., 2016. Biosens. Bioelectron. 86, 1074–1079.
Cincotto, F.H., et al., 2016. Talanta 147, 328–334.
Dutta, G., et al., 2017. Biosens. Bioelectron. 92, 372–377.
Gasparotto, G., et al., 2017. Mater. Sci. Eng. C 76, 1240–1247.
Giannetto, M., et al., 2011. Biosens. Bioelectron. 26, 2232–2236.
Hu, X., et al., 2016. Electrochim. Acta 187, 560–566.
Jiang, P., et al., 2010. J. Am. Chem. Soc. 132, 2858–2859.
Kavosi, B., et al., 2014. Biosens. Bioelectron. 59, 389–396.
Khetani, S., et al., 2018. ACS Sens. 3, 844–851.
Khoshroo, A., Mazloum-Ardakani, M., Forat-Yazdi, M., 2018. Sens. Actuators B: Chem. 255, 580–587.
Kraus, J., Böbel, M., Günther, S., 2016. Carbon 96, 153–165.
Li, F.Y., et al., 2015. Biosens. Bioelectron. 68, 626–632.
Moazeni, M., Karimzadeh, F., Kermanpur, A., 2018. Biosens. Bioelectron. 117, 748–757.
Natarajan, A., et al., 2017. Sci. Rep. 7, 11.
Preechakasedkit, P., et al., 2018. Biosens. Bioelectron. 102, 27–32.
Rettew, R.E., Allam, N.K., Alamgir, F.M., 2011. ACS Appl. Mater. Interfaces 3, 147–151.
Samanman, S., et al., 2015. Anal. Chim. Acta 853, 521–532.
Serafin, V., et al., 2018. Talanta 179, 131–138.
Shamsipur, M., et al., 2018. Biosens. Bioelectron. 103, 54–61.
Strauss, V., et al., 2018. Adv. Mater. 30, 1704449.
Tian, Y., Tatsuma, T., 2005. J. Am. Chem. Soc. 127, 7632–7637.
Wang, Y., et al., 2018. Biosens. Bioelectron. 106, 179–185.
Xu, T., et al., 2017. Biosens. Bioelectron. 95, 87–93.
Yin, H., et al., 2017. Biosens. Bioelectron. 90, 494–500.
Zhang, X., et al., 2018. Biosens. Bioelectron. 106, 142–148.
Zhao, J.Q., et al., 2015. Microchim. Acta 182, 2435–2442.